A non-local approach to model the combined effects of forging defects and shot-peening on the fatigue strength of a pearlitic steel

Benjamin Gerin, Etienne Pessard, Franck Morel, Catherine Verdu

A non-local approach to model the combined effects of forging defects and shot-peening on the fatigue strength of a pearlitic steel

Benjamin Gerin[a,b,], Etienne Pessard[a], Franck Morel[a], Catherine Verdu[b]

[a]*LAMPA, Arts et Métiers ParisTech Angers, 2 Bd du Ronceray, 49035 Angers Cedex 01, France*
[b]*MATEIS, INSA de Lyon, Bâtiment St Exupery, 20 av Jean Capelle, 69621 Villeurbanne Cedex, France*

Abstract

This study focuses on the influence on fatigue behaviour of the surface integrity of a steel connecting rod. The component is hot-forged and shot-blasted, producing a complex surface state with large surface defects and high residual stresses. In a prior study, the surface was thoroughly characterized and fatigue tests were performed. Several different surface states were analysed in order to quantify the influence of the various surface aspects. These tests showed that the forging defects and the residual stresses are the most influential aspects of the surface. The goal of this paper is to develop an approach capable of taking into account the influence of both these aspects on fatigue behaviour.

Two methods were developed. First, using surface scans of the fatigue specimens, the forging defects were fitted with ellipsoids so as to determine their size and shape. This allows to easily compare the numerous defects and test various criteria in order to identify the critical defect of each specimen. The second method used was the finite element simulation of the defects based on real topography scans. Using a non-local approach based on the theory of critical distances, the simulations were used to accurately predict the influence of the defects' geometry. The residual stress profiles were integrated in the simulations using Dang Van's criterion. The predictions are accurate and show the importance of taking into account the real defect geometry when estimating the fatigue strength.

Keywords: Steel, Forging, Shot-peening, High Cycle Fatigue, Surface Defects, Non-local Approach

Email address: benjamin.gerin@ensam.eu (Benjamin Gerin)

1. Introduction

The high cycle fatigue behaviour of industrial components can be affected by material characteristics but also by the production process. These elements must be taken into account during the design process.

Because crack initiation is usually located at the surface, a large number of articles in the literature focus on how surface integrity affects fatigue behaviour. The term "surface integrity" includes various aspects that can all affect fatigue behaviour:

- Surface roughness
- Surface defects
- Residual stresses
- Hardening
- Microstructure

Surface integrity is very dependant on the process being used, so studies on this subject usually focus on a specific process: machining [1, 2, 3], stamping [4], punching [5]. A large number of papers also deal with the impact of localised natural or artificial defects on fatigue strength. A classic example is Murakami's work [6, 7]. More recently, studies have been performed on steel [8, 9, 10], on cast iron [11, 12, 13], on cast aluminium alloys [14, 15, 16] and cast titanium alloys [17]. Most investigations on defects are performed on homogeneous materials, without residual stresses. However, in the case of hot-forged steel, shot-blasting is generally used to clean off the scale. Shot-blasting is akin to shot-peening and affects surface integrity by introducing residual stresses, hardening and surface damage, and changing the microstructure. Numerous articles have been published on how shot-peening affects surface integrity and fatigue behaviour. Gariépy et al. [18] conducted a thorough characterisation of the surface of a shot-peened aluminium. Bhuiyan et al. [19] investigated shot-peened magnesium alloy specimens, some of which were stress-relieved after peening. McKelvey & Fatemi [20] studied the effects of decarburisation and shot-cleaning of the surface of steel specimens. Sakamoto et al. [21, 22] studied the influence of surface cracks introduced by shot-peening on steel specimens Kim et al. [23] showed that in high cycle fatigue, surface residual stresses show little stress-relief during fatigue cycling.

In order to take into account the influence of the various aspects of the surface integrity, different approaches have been suggested. The majority of the studies on the effect of surface integrity on fatigue behaviour are performed on machined components. Machined surfaces typically have a periodic roughness profile. Arola & Ramulu [24] have therefore suggested a model based on the roughness values and on the estimation of the stress concentration factor suggested by Peterson [25]:

$$K_f = 1 + q(K_t - 1) \quad \text{with} \quad K_t = 1 + n\left(\frac{R_a}{\rho}\right)\left(\frac{R_y}{R_z}\right) \quad \text{and} \quad q = \frac{1}{1 + \gamma/\rho} \tag{1}$$

where ρ is the notch curvature radius and (n, γ) are material parameters. Extending this model, Suraratchai et al. [26] suggested estimating the stress concentration with 2D simulations of the roughness profiles. Using 3D simulations from 3D surface scans to estimate the stress distribution was first performed by Shahzad and then used on surface states from other processes like forging or punching [5]. Guillemot and Souto Lebel suggest taking into account the stress concentration using a statistical model which considers micro-defects as pre-existing population of defects. Also worth mentioning is the original work of Le Pecheur [27] and Guilhem [28] based on evaluating the surface effects using crystal plasticity. When studying defects, the Kitagawa-Takahashi diagram [29] is a very useful tool, as it allows to illustrate the effect of defect size on the fatigue strength.

Fathallah et al. [30] studied the effect on fatigue behaviour of shot-peening coverage (100% or 1000% surface coverage). To model the fatigue behaviour, they performed 2D finite element simulations, taking into account the specimen geometry, the surface defects, the surface damage, the residual stresses and the hardening introduced by shot-peening. To study the influence of surface defects, other authors have used non-local approaches based on the theory of critical distances defined by Taylor [31, 32]. This method has the advantage of using the elastic stress distribution to predict fatigue strength. It has been used in a number of applications [33, 34], such as welded joints [35, 36], fretting [37], cast alumium [38], punching defects [5], corrosion defects [39] and vapour deposition defects [40]. This approach has been combined with a multiaxial fatigue criterion and applied to shot-peened specimens [41]. It has also been used to develop a non-local damage model for shot-peened turbine blades [42].

The component studied in this paper is a hot-forged connecting rod, which is shot-blasted after forging. The connecting rods therefore exhibit localised surface defects introduced during forging in addition to hardening and residual stress gradients generated by the shot-blasting. The goal of this paper is to develop a fatigue approach which can account for the specific surface integrity of hot-forged and shot-peened components. This work is based on the results of a large experimental campaign, detailed in a previous article [43]. The various studied surface states and the fatigue results will first be quickly summed up. These results will then be used to model the fatigue behaviour of the specimens. Two approaches will be detailed in this article. The first uses ellipsoids to fit the shape and size of the forging defects present on the fatigue specimens. The defect dimensions are then used to try and detect the critical defect and its fatigue strength. In addition, the statistics of extremes are used to predict defect sizes on larger sample sizes. The second approach is based on finite element (FE) simulations using the geometry of real defects. The theory of critical distances combined with the residual stress profiles is used to predict the specimen's fatigue strength.

2. Fatigue testing results

In the previous study, fatigue specimens were machined out of connecting rods (figure 1a). Several different surface states were analysed in order to quantify the influence of the various aspects of surface integrity. The various surface states used in this study are as follows:

- As-forged surface, manually cleaned of scale
- Shot-blasted, the surface state of industrially produced connecting rods
- Shot-peened with shot diameter 800 μm, Almen intensity 30–60 A with 200% coverage. This shot-peening was performed on as-forged specimens and was chosen so as to be as close as possible to the shot-blasted surface.
- Shot-peening with shot diameter 400 μm, Almen intensity 20–30 A with 200% coverage. This shot-peening was performed on as-forged specimens and was chosen so as to have a lower roughness and a shallower residual stress profile.
- Polished, used as the reference in fatigue

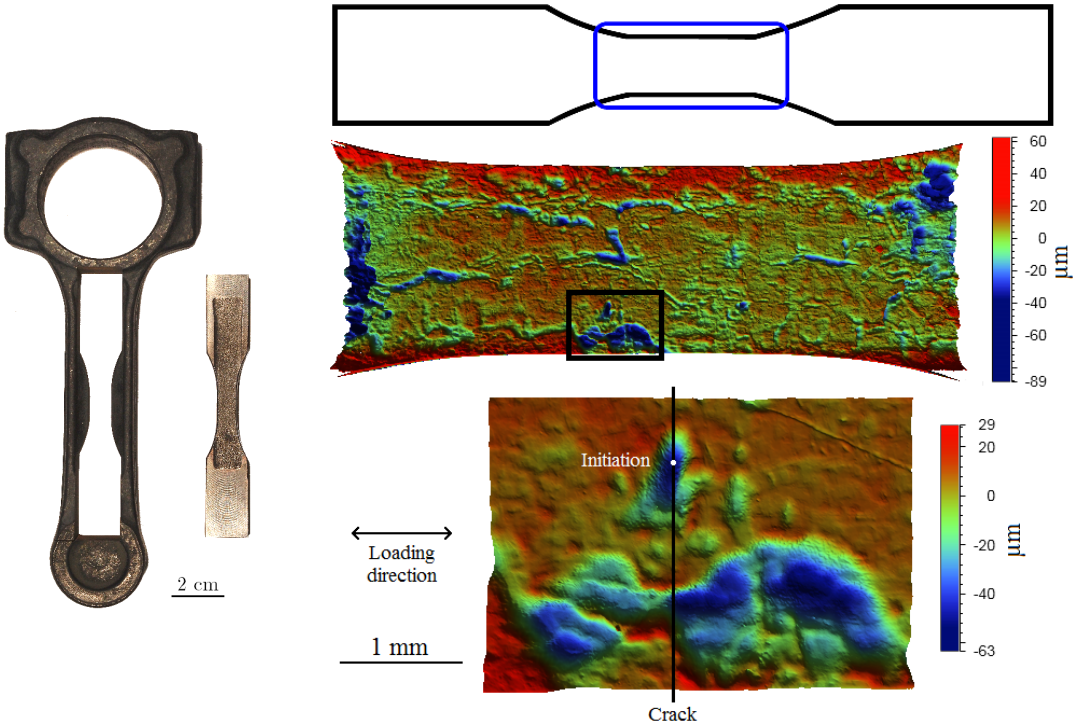

Fig. 1: a) Connecting rod with spark-machined specimen. b) Example of a critical defect on an as-forged specimen. [43]

The surface of the specimens was scanned using a profilometer prior to fatigue testing. This allowed the identification of the critical defect (the defect where crack initiation occurred) for each specimen. Figure 1b shows the crack path and the critical defect for an as-forged specimen. In addition to the surface topography, the hardness, residual stresses and microstructure gradients were analysed. Figure 2 shows the residual stress profiles of all batches. Additional information on the preparation and the analysis of the specimens can be found in the article [43].
Fatigue test were performed in plane bending with a load ratio $R = -1$. Some specimens were stress-relieved in tension prior to fatigue testing, in order to quantify the influence of the residual stresses. Fatigue tests were also performed in tension $R = -1$. However, not all specimens were valid as crack initiation sometimes occurred in the corner. Only one of the tension tests was valid, performed on a stress-relieved shot-peened ∅800 µm shot, all the others had a corner crack initiation.

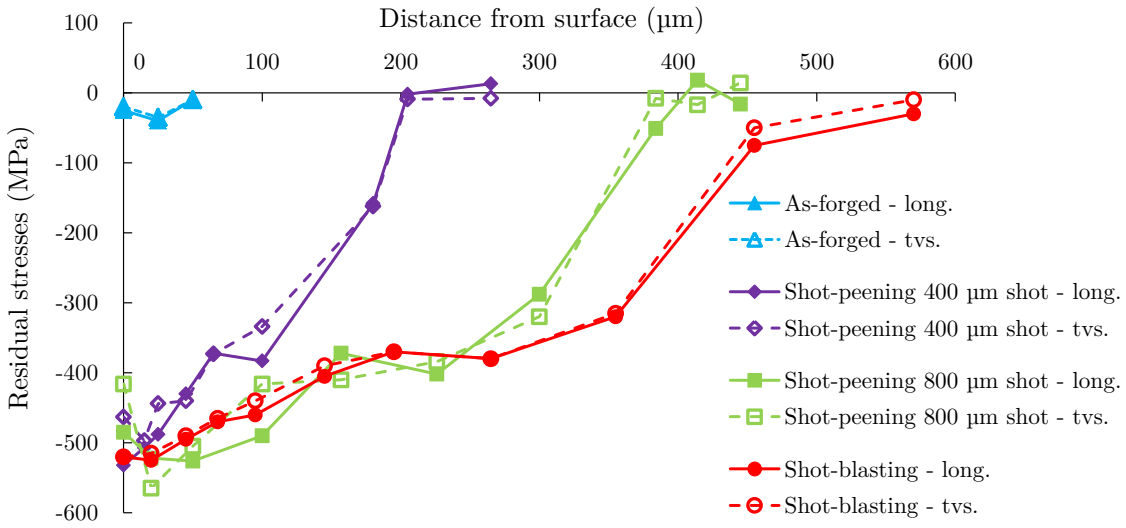

Fig. 2: Residual stress profiles for the various batches, in the direction of the specimen axis (long.), and the transverse direction (tvs.). [43]

Table 1 details the number of valid specimens for each batch, with their respective fatigue strength range. The average value from the staircase method on the polished specimens is the

Batch	Test type	Nbr. of specimens	σ^D (MPa)
Polished	Staircase	15	424
As-forged	Locati	34	280–400
Shot-blasting	Locati	8	420–500
Shot-peening ∅800 µm shot	Locati	10	500–580
Shot-peening ∅400 µm shot	Locati	18	400–500
Tension SP ∅800 µm shot **stress-relieved**	Locati	1	431

Table 1: Overview of the number of valid tests and fatigue strength range for each batch. [43]

reference fatigue strength of the material: $\sigma_0^D = 424$ MPa.

Crack initiation for valid specimens was always located on a large forging defect. The fatigue results for all specimens are represented in a Kitagawa diagram (figure 3). Defect size is represented using the square root of their surface area, projected along the loading direction [6]. The fracture surfaces can be used to calculate the projected surface area of each critical defect,

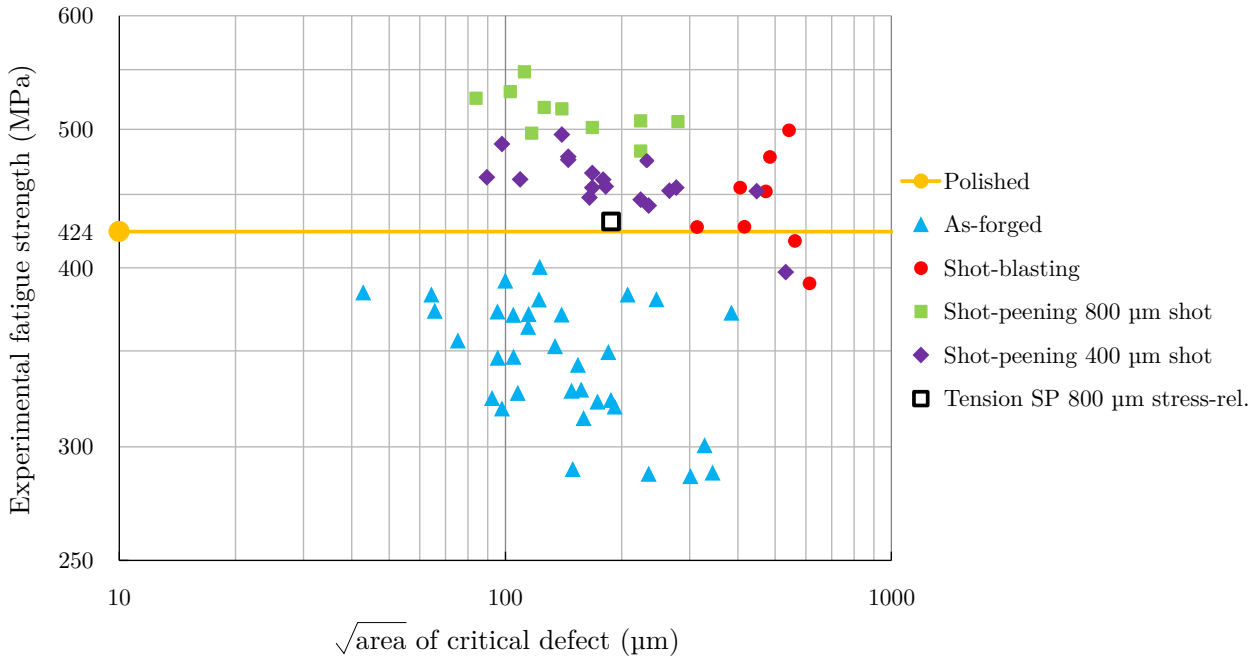

Fig. 3: Kitagawa diagram of the fatigue tests, with fatigue strength and critical defect size of each valid specimen. [43]

which is generally used to represent defect size. All the defects have a projected area of similar shape, with the width much bigger than the depth (defects are typically 500–2000 µm wide and 50–200 µm deep). Calculating the projected area is done using the SEM fracture surface images: the total width and maximum depth of the defects are measured and their projected surface area is calculated by supposing that they have a semi-elliptical shape. As suggested by Murakami, the defect width is limited by a threshold of 10 times the depth when calculating the projected area. The fatigue results show that:

- **Forging defects play a significant role in fatigue.** Crack initiation was always located on a forging defect. The as-forged specimens all have a lower fatigue strength than the reference fatigue strength because of the defects. Furthermore, all batches are influenced by defect size: larger defects lead to lower fatigue strength.
- **Shot-blasting and shot-peening improve fatigue strength significantly.** Shot-blasting and shot-peening increase the fatigue strength by approximately 150 MPa compared to the as-forged specimens (for similar defect sizes). This increases the fatigue strength much

higher than the reference, despite the influence of defects. The two shot-peened batches do not have quite the same fatigue strength, with the ∅400 µm shot being around 50 MPa lower.

- **Residual stresses have a major influence.** The stress-relieved specimen shows a significant drop (70 MPa) in fatigue strength compared to the other specimens of the same batch. This drop is only due to the absence of the residual stresses in the loading direction, as no other aspect of the surface integrity was changed.

The fatigue results show that the forging defects and the residual stresses are the two features of the surface integrity that have the most influence on fatigue behaviour.
The experimental part of the study has already been performed and published [43]. This article will therefore focus on establishing a fatigue model taking into account influence of the surface integrity.

3. Geometrical analysis of the surface defects

The specimen's surface contains numerous forging defects, all with a unique shape and size. These defects do not all have the same influence in fatigue and it is therefore of interest to be able to determine the most harmful defect (the critical defect) *a priori*. The fatigue results show that the critical defect is not necessarily the deepest or the largest defect. Furthermore, the forging defects usually form complex networks in which individual defect are not easily isolated.
In order to simplify the analysis of the defects, their geometry will be approximated using an ellipsoid. The ellipsoid shape is chosen because most defects are much larger than they are deep and are very smooth, with the deepest point near the center of the defect. Each defect is therefore approximated by a half-ellipsoid defined by three parameters (a, b, c), the semi-axes of the ellipsoid, which represent the length, width, and depth of the defect. The dimensions of the ellipsoid are then used to determine the defect's influence in fatigue. To simplify the fitting of the ellipsoid, the center of the ellipsoid and its semi-axes a and b are locked parallel to the surface. The semi-axis c is therefore parallel to the z axis and the orientation of the ellipsoid is defined by a single angle. In order for the ellipsoid to correctly represent the depth of the defect, the value of

the semi-axis c is set to the maximum depth of the defect. Each defect can thus be represented by an ellipsoid using only four parameters: the three semi-axes (a, b, c) and θ, the angle between the major semi-axis a and the loading direction x (figure 4). To limit the total number of defects per

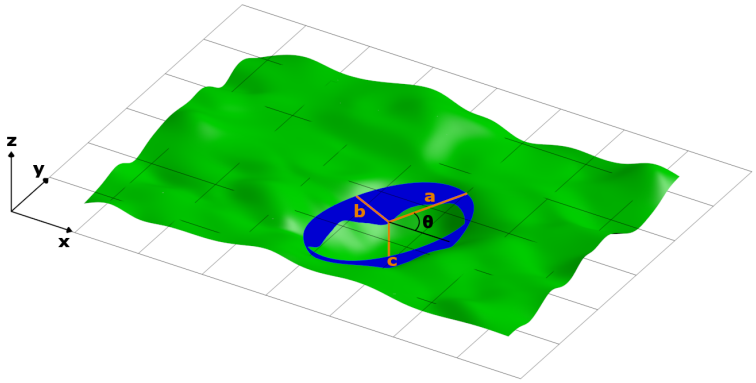

Fig. 4: Diagram of a surface with a defect (green) and the corresponding ellipsoid (blue). The grid is the reference plane.

specimen, only defects deeper than 15 µm are analysed. Using this method, approximately 100 defects were detected per specimen, on average.

In order for the ellipsoid to reflect the defect geometry as accurately as possible, the ellipsoids are fitted using the least squares method. A second ellipsoid is fitted on an area restricted to a 100 µm radius around the defect's deepest point. This second ellipsoid is mostly useful in the case of larger defects, for which the general shape does not necessarily reflect the geometry at the bottom of the defect. Values for the radius ranging from 50 to 200 µm were tested without any noticeable improvement of the results. The intermediate value of 100 µm was therefore chosen. Figure 5 shows a defect from an as-forged surface with the two fitted ellipsoids.

The method used to detect the defects supposes that the crack initiation point is located in the deepest part of the defects. However, for two of the 34 as-forged specimens, crack initiation was located in a shallow area connected to a larger and deeper defect. For these two specimens (n°13 and 21), the algorithm was not able to correctly fit the critical area as it ignored the shallow crack initiation area in favour of the deeper, non-critical part of the defect.

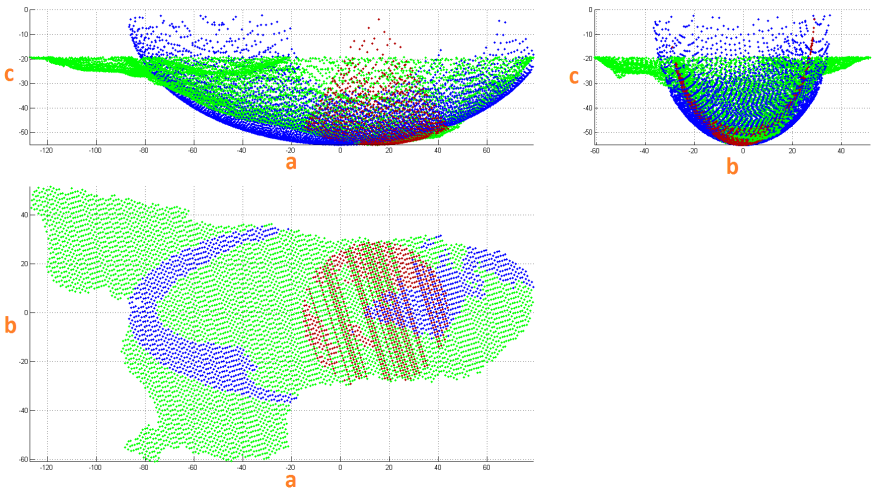

Fig. 5: Example of a surface defect (green) with the fitted ellipsoids (blue and red). The values for the semi-axes a and b are given in pixels (1 pixel = 3.5 µm) and the values for c are in µm.

3.1. Detecting the critical defect

This method analyses both critical and non-critical defects, which means it is possible to compare them in order to detect the critical defects on the specimens' surface. The classical criterion used to compare defects is the projected area, as used in Murakami's model. An ellipsoid's maximum cross-section contains its center and has the shape of an ellipse, making it easy to calculate its projected area. The projected area is calculated using the total length and the depth of the large ellipsoid. As before, a length threshold of 10 times the depth is applied when determining the projected area. Figure 6 compares, for each as-forged specimen, the projected area of the critical defect with that of every other defect. According to Murakami's model, defects with the greatest projected area are the most influential in fatigue. The critical defects of the as-forged specimens have mostly high projected areas compared to the other defects. However, the critical defect has the highest area for only six of the 32 as-forged specimens. The same results are observed for the shot-peened specimens. This confirms prior observations on as-forged specimens where the critical defect is smaller in size to other defects [43]. This means that the square root of the projected area cannot be used to accurately detect the critical defect.

Peterson's criterion [25] gives a defect's stress concentration factor, K_t, using the defect's depth c

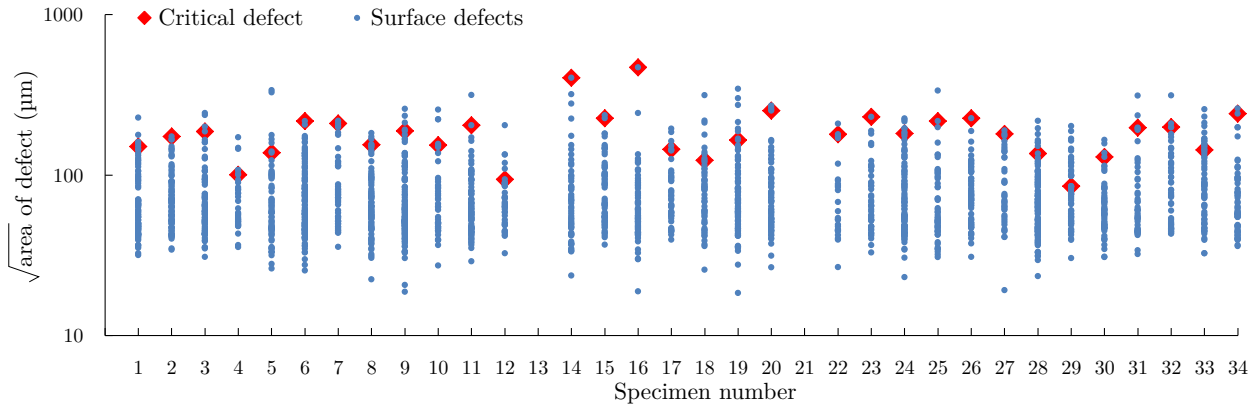

Fig. 6: $\sqrt{area}$ of the defects from the as-forged specimens. For each specimen, the blue point are the defects and the critical defect is marked in red.

and its curvature radius ρ in the loading direction:

$$K_t = 1 + 2\sqrt{\frac{c}{\rho}} \tag{2}$$

An ellipse's curvature radius is easily calculated. In the case of the ellipse along the loading direction:

$$\rho_x = \frac{(\text{semi-axis}_x)^2}{c} \tag{3}$$

The curvature radius at the bottom of the defects can thus be calculated using the semi-axes of the small ellipsoid.

Figure 7 compares the K_t of all defects for every specimen. For the as-forged and shot-peened batches, the critical defect has the highest K_t of all defects for roughly a third of all specimens. In the case of the shot-blasted specimens, the critical defects' large size make them easily identified (this batch has large uniformly large defects because of choices made during fatigue testing [43]). The K_t is therefore a better criterion for detecting the critical defects than the projected area, but is not able to detect all critical defects. There are several possible explanations for this:

- The K_t is calculated using the curvature radius of the small ellipsoid fitted at the bottom of the defects. This means that most of the defect geometry is ignored in favour of the deepest part.

- The 100 μm radius value might not be the best choice, however, tests with different values have shown no improvement of the results.
- Defects can be close together and thus interact with each other. Each defect is analysed independently and thus potential interactions are ignored.

In order to predict the fatigue limit, Peterson gives an empirical relationship using the K_t to calculate a K_f (defined as $K_f = \sigma_0^D / \sigma_{\text{defect}}^D$):

$$K_f = 1 + q(K_t - 1) \text{ with } q = \frac{1}{1 + \gamma/\rho} \tag{4}$$

γ is a material parameter. γ can be fitted with the least squares method, using the experimental results. The value thus obtained is $\gamma = 1.01$ (with ρ in mm).
When compared to the fatigue results, the K_f values of the critical defects of the as-forged specimens have an average error of 8% with a maximum error of 19%. However, when comparing all defects together in order to detect the critical defects, the K_f is a less effective criterion than K_t.

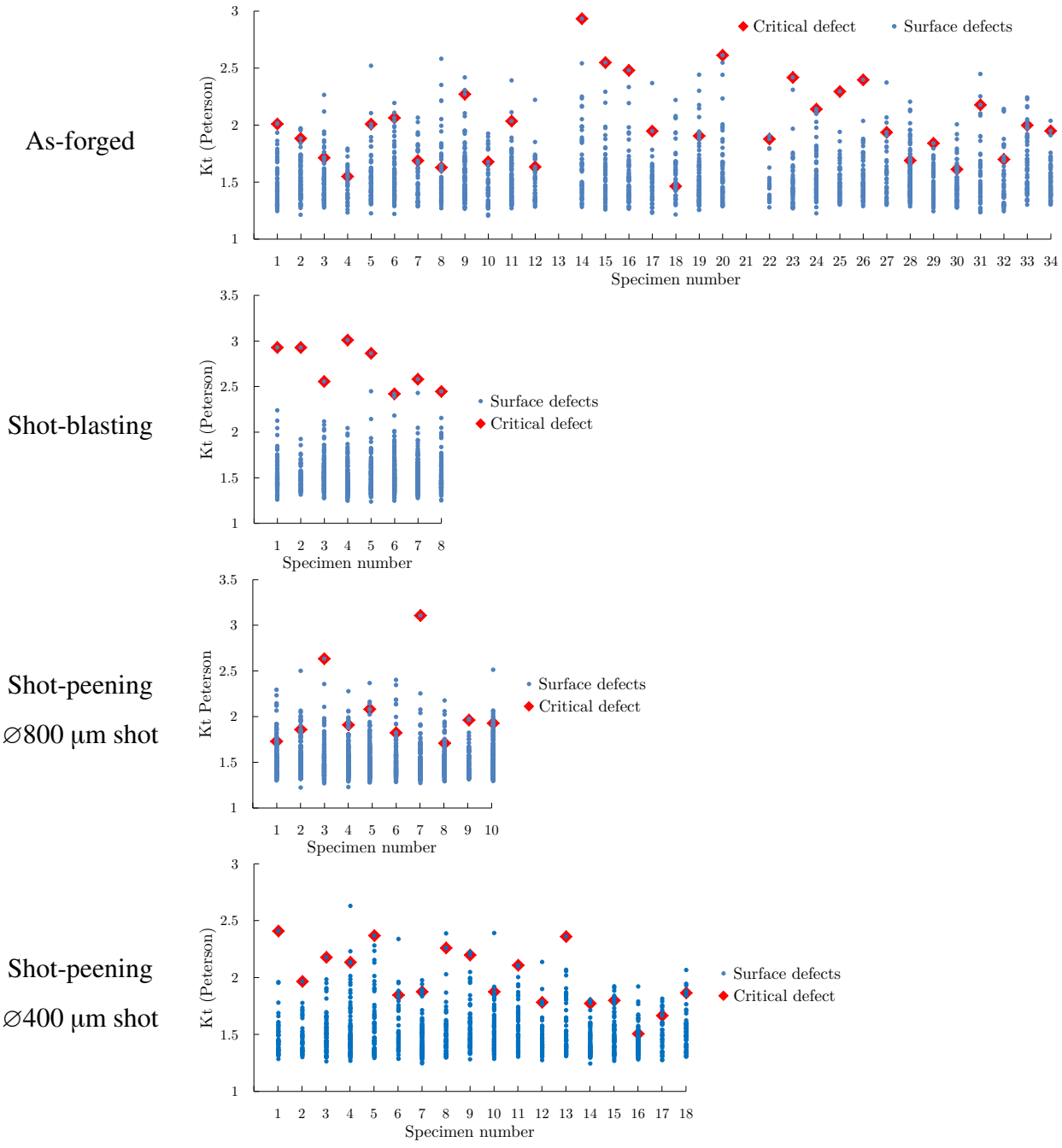

Fig. 7: Peterson's K_t of each defect for all specimens. For each specimen, the blue point are the defects and the critical defect is marked in red.

3.2. Predicting the maximum defect size on a larger sample

The present study is performed on less than a hundred specimens when the industrial production of forged components can be in the millions. The number of analysed critical defects is too small to be a representative sample. Furthermore, the critical defects have the most impact in fatigue and are therefore in the tail of the defect distribution. The statistics of extremes, defined by Gumbel [44], are used to study statistically rare events. This approach has been used by other authors to study defects in fatigue, for example Murakami [45]. The method is applied with the following steps:

- Define a reference area S_0 and determine the studied event's distribution by identifying the most extreme event on N samples of size S_0
- Verify that the distribution of the studied events has indeed the same form as Gumbel's distribution
- If it is the case, determine the (λ, δ) parameters of the distribution
- Use the return period to predict the extreme events on a larger sample

Gumbel's cumulative distribution function is:

$$F(A_{\max}) = \exp\left(\exp\left(\frac{-(A_{\max} - \lambda)}{\delta}\right)\right) \tag{5}$$

where $A_{\max}$ is the studied event (for example, the critical defect's projected area or its K_t), and (λ, δ) are the parameters for the distribution. In order to compare the distributions, the standardised variable y is introduced:

$$y = \frac{A_{\max} - \lambda}{\delta} \tag{6}$$

The cumulative distribution function can then be expressed as $F(y) = \exp(\exp(-y))$ and the standardised variable as $y = -\ln(-\ln(F(y)))$. The linear relationship between y and $A_{\max}$ in equation (6) means that Gumbel's distribution is a line in a y versus $A_{\max}$ plot.
Each event for the N observations are sorted and numbered in increasing order: $A_{\max,j}$ with j from 1 to N. For each numbered event, the corresponding cumulative probability is:

$$F_j = \frac{j}{N+1} \tag{7}$$

the corresponding standardised variable is $y_j = -\ln(-\ln(F_j))$. If the extreme events follow Gumbel's distribution, then plotting the $(A_{\max,j}, y_j)$ points will show a linear relationship. Using equation (6), it is therefore possible to determine the distribution's (λ, δ) parameters. The distribution can then be used to predict extreme events on larger sample sizes.

To estimate the extreme event on a surface $S > S_0$, Gumbel uses the concept of return period, defined as $T = S/S_0$, the associated cumulative probability is:

$$F_S = \frac{T-1}{T} \tag{8}$$

The most extreme event on the surface S is then estimated with:

$$A_{\max,S} = \lambda + \delta\, y_S \tag{9}$$

where $y_S = -\ln(-\ln(F_S))$.

In our case, the samples are the fatigue specimens, the reference area S_0 is therefore the surface area of the central part of the specimens (twice 20×6.5 mm, top and bottom). The extreme event is the critical defect, there is only one per specimen and it is determined by the fatigue tests. The defects can be quantified using different parameters (depth, projected area, K_t, etc.), however not all parameters follow Gumbel's distribution. Figure 8 shows the standardised variable plots for the K_t and the depth of the critical defects of the as-forged specimens. The K_t follows Gumbel's

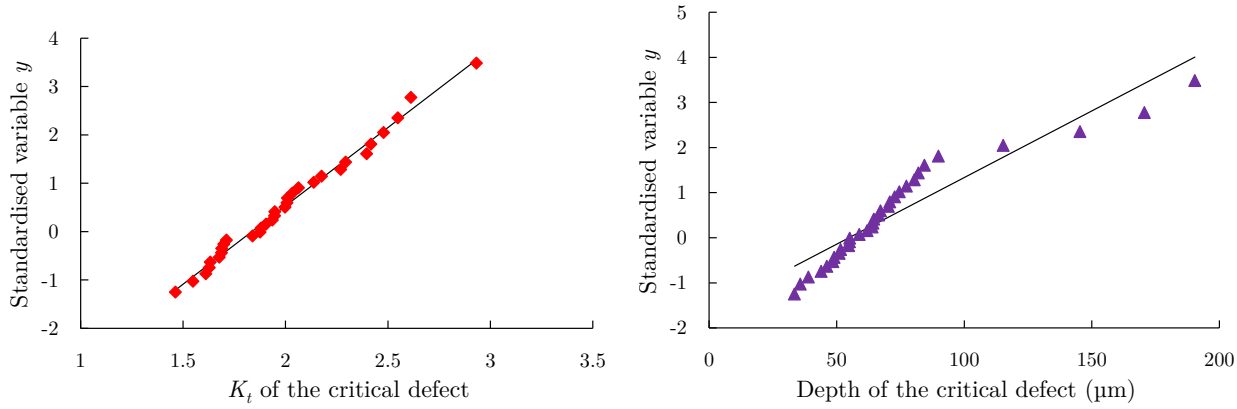

Fig. 8: Plots versus the standardised variable of the critical defects' K_t and depth values. The K_t values follow a Gumbel distribution (straight line), but the depth does not.

distribution, but the depth does not. The parameters for the K_t distribution can be calculated with equation (6), and the maximum K_t on a larger sample can be predicted with equation (9). The reference surface being one specimen, the return period T can be considered to be the total number of specimens in the larger sample. The predicted maximum K_t for 10^6 is: $K_{t,10^6} = 6.1$. This method can be used to predict defect size on entire industrial productions, without having to individually check every component.

Comparing the K_t to the projected area, not only is the K_t a better criterion for detecting the critical defect, it also follows Gumbel's distribution. In an industrial context, where fatigue tests cannot be performed on all components, the K_t is therefore the best criterion for the analysis in fatigue of forging defects.

4. Finite element simulations of the critical defects

Fitting the defects with ellipsoids allows to model the effect of their geometry in fatigue but ignores other aspects of the surface integrity, specifically those of shot-peening. The fatigue tests have shown that the two most important aspects of surface integrity are the defects and the residual stresses introduced during shot-peening and shot-blasting. Finite element simulations allow to more accurately model their influence on fatigue behaviour:

- The geometry of the defect is directly used in the FE simulation, with no simplification or approximation.
- Interactions between defects can be taken into account if the simulated area is large enough.
- Integrating the residual stress profile into the FE simulations allows the accurate analysis of its influence.

4.1. FE modelling of the forging defects

The simulations are performed using the surface scans of the defects. The surfaces of the specimens are too large to be simulated in their entirety, therefore the defects are simulated independently. Because of the large number of defects, the simulations are restricted to only the critical defects. If large defects are close to the critical defect, these are included in the simulation in order to take into account eventual interactions.

The scans are simulated with a thickness of 2 mm (the specimens have a total thickness of around 6 mm). The elements are linear tetrahedra, meshing is performed using the GMSH software [46], with a element size gradient in order to reduce the number of elements. Mesh size at the surface (top) is 7 µm, gradually increasing to a size of 1 mm at the bottom (figure 9). With these meshing

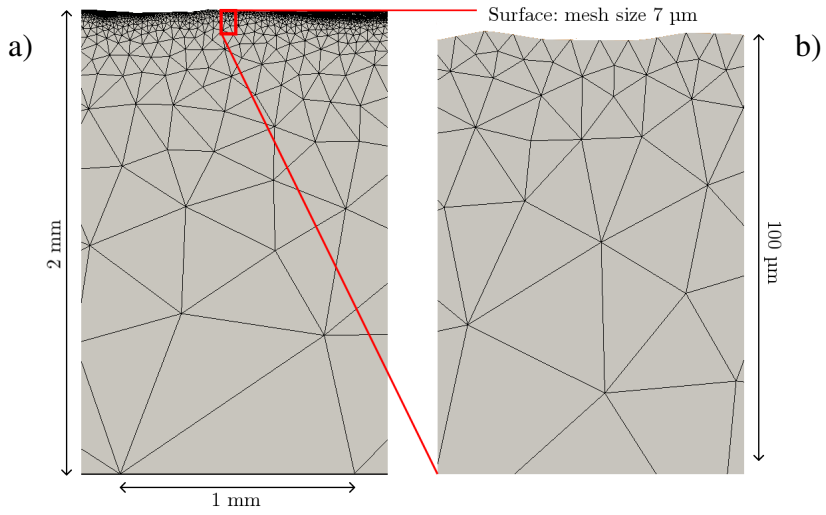

Fig. 9: Close-up of the mesh showing the element size gradient. a) Mesh gradient along the entire thickness. b) Mesh gradient in the first 100 µm, surface is marked in orange.

parameters, a 2×2 mm scanned surface results in a mesh with approximately 400 000 elements. Solving was performed using a software developed at LAMPA. More information about the solver can be found in the article by Robert & Mareau [47].

The loading conditions are given in figure 10.

Previously performed analysis of the residual stresses during fatigue cycling have shown that there is no residual stress relaxation, even in the forging defects [43]. This indicates that there is very little plastic strain at the surface, an elastic behaviour is thus used for the simulations. The cyclic fatigue loading is simulated using a single step of equal load.

Figure 11 shows the various steps used to perform FE simulations of the critical defects.

Figure 12 compares the surface scan of a critical defect with the surface stress values obtained through FE simulation. The simulation correctly identifies the critical defect and, in this particular case, the K_t values calculated with the ellipsoids are very close to the results of the FE simulation.

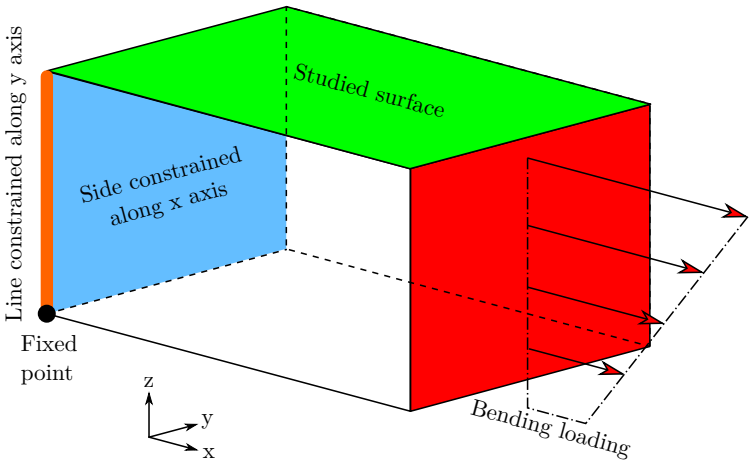

Fig. 10: Loading conditions of the FE simulations.

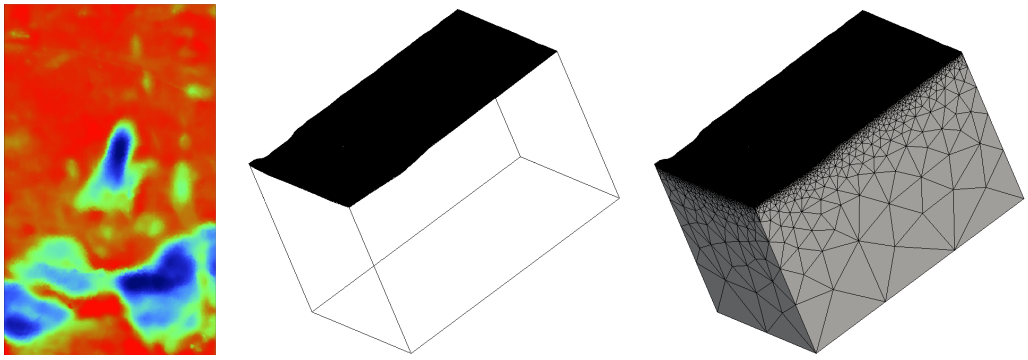

1) Surface scan 2) Surface meshing 3) Volume meshing

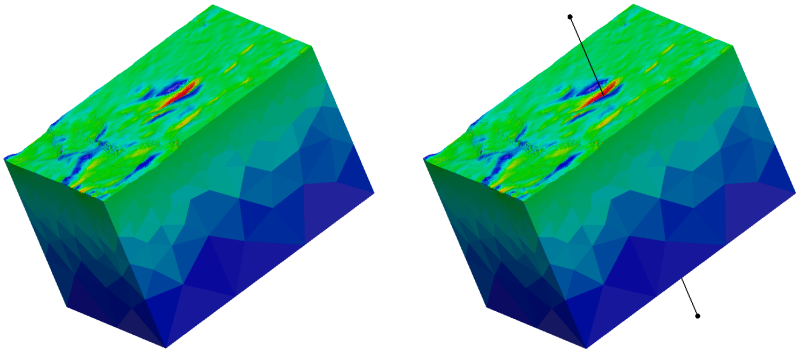

4) FE simulation 5) Application of fatigue model

Fig. 11: Process for performing the FE simulations of the critical defects.

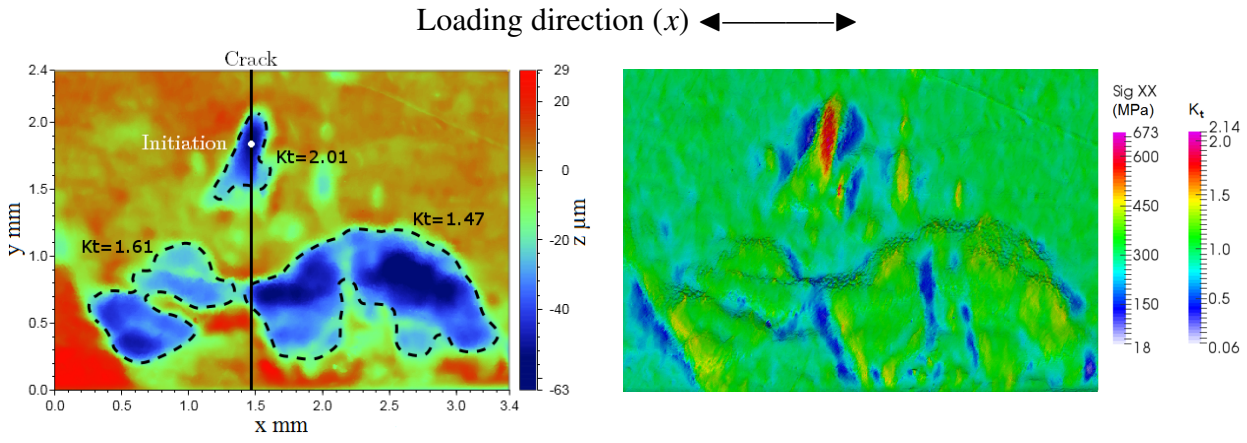

Fig. 12: FE simulation of a critical defect compared to its surface scan. Indicated on the scan are the defects' K_t value, calculated using the geometrical analysis.

4.2. FE fatigue model

The surface K_t values calculated through the FE simulations cannot be directly used to predict fatigue strength. Furthermore, due to notch effect, these values are heavily dependent on the surface mesh size. Another method is therefore required to accurately predict fatigue strength. In order to model the shot-peened and shot-blasted specimens, the residual stresses must be taken into account. The Dang Van criterion [48] can be used to integrate the residual stresses in the stress value obtained with the point or volume methods. In the case of a proportional uniaxial loading, the criterion is written as:

$$\tau_a + \alpha\,\sigma_{\mathrm{H,max}} \leqslant \beta \tag{10}$$

where τ_a is the shear stress amplitude, $\sigma_{\mathrm{H,max}}$ is the maximum hydrostatic stress and (α, β) are material parameters. The residual stresses are constant during cycling and can therefore be integrated into the hydrostatic stress. The defect geometry will locally affect both τ_a and $\sigma_{\mathrm{H,max}}$, proportionately to the loading stress. In this way, the model takes into account both the defect's geometry and the residual stresses. In the case of the polished specimens, there are no defects and no residual stresses, the local stress tensor is therefore equal to the loading stress: σ_0^D, and equation (10) can be written as:

$$\frac{\sigma_0^D}{2} + \alpha\frac{\sigma_0^D}{3} = \beta \;\Rightarrow\; \sigma_0^D = \frac{\beta}{1/2 + \alpha/3} \tag{11}$$

For the shot-peened and shot-blasted specimens, the residual stresses along the vertical axis are considered negligible, the residual stress tensor is therefore:

$$\sigma^{\mathrm{RS}} = \begin{pmatrix} \sigma_{11}^{\mathrm{RS}} & 0 & 0 \\ 0 & \sigma_{22}^{\mathrm{RS}} & 0 \\ 0 & 0 & 0 \end{pmatrix} \tag{12}$$

The residual stress analysis has shown that they are equi-biaxial, as shot-peening and shot-blasting do not favour a particular direction.

Different criteria were tested and the chosen model is based on the theory of critical distance [31]. Instead of using the surface stress, this model uses the stress a depth d below the defect and compares it directly to the reference fatigue stress σ_0^D. The critical distance d is a material

parameter. In the case of an elastic simulation, this means that a K_f value can be directly determined by comparing the stress at the critical distance with the loading stress. Several methods are available for calculating the stress at the critical distance. The simplest is the point method, where the stress is simply the stress value at a single point located at the distance $d/2$ beneath the tip of the defect. The volume method requires averaging the stress values in a sphere of radius d centred on the tip of the defect. Figure 13 shows an example of both methods being applied to a critical defect.

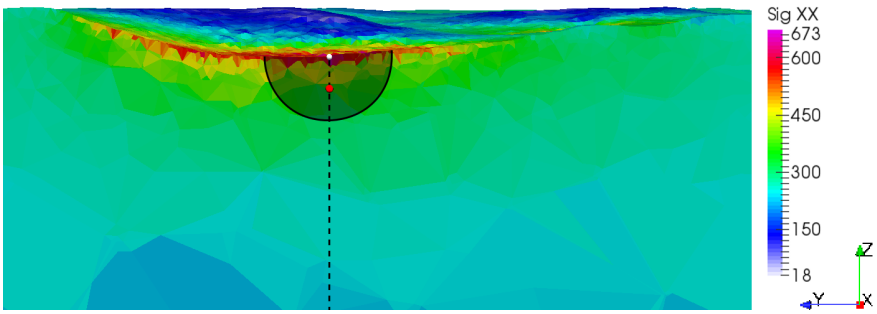

Fig. 13: Cross-section of the FE simulation of the critical defect in figure 12. Stress values are in MPa, the white dot locates the maximum stress. The point method (red dot) and volume method (sphere centred on the white dot) are indicated.

As the point and volume methods give very similar results, only point method results will be presented in this article. For the point method, the contribution of the residual stresses is obtained simply by using the residual stress values at the depth $d/2 = 40$ µm. These values are:

- Shot-blasting: 500 MPa
- Shot-peening ∅800 µm shot: 525 MPa
- Shot-peening ∅400 µm shot: 445 MPa

4.3. Determining the critical distance and the (α, β) parameters

The critical distance is a material parameter, and therefore should change during shot-peening or shot-blasting. However, the most important aspects in fatigue being the defects and the residual stresses, the critical distance and other material parameters are considered equal to the as-forged values for the sake of simplicity.

The critical distance d is determined using the critical defects of the as-forged specimens. Each critical defect is loaded with its respective fatigue limit, ranging from 286 to 400 MPa, and the stress gradient below the maximum surface stress value is plotted. Because the defects have different depths, varying from 31 to 171 µm, the gradients are plotted in relative depth, with 0 depth being the surface. The resulting stress gradients are plotted in figure 14. According to the

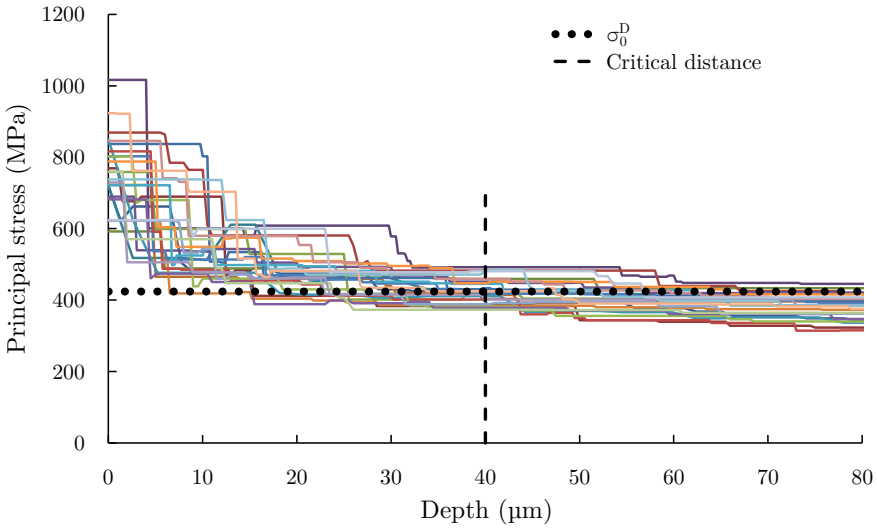

Fig. 14: Stress gradients below the maximum stress for all critical defects of the as-forged specimens. Depth is relative: for each gradient, 0 depth is the tip of the defect.

point method, the stress values are the closest to the reference fatigue strength σ_0^D at the depth $d/2$. The stress values are closest to σ_0^D at a depth of 40 µm, resulting in a critical distance of 80 µm.

In order to apply the Dang Van model, the (α, β) parameters must be determined. If we assume that the (α, β) values are independent of the hardening, then all batches have identical parameters. Using the FE simulations of all specimens, it is therefore possible to determine the (α, β) pair that gives the overall best fit of the experimental results. The values obtained this way are: $\alpha = 0.27$ and $\beta = 250$ MPa.

4.4. Results and discussion

Figure 15 plots the predicted versus experimental fatigue strengths for all critical defects of all batches (point method). The simulations correctly predict the fatigue limit, with only a few points

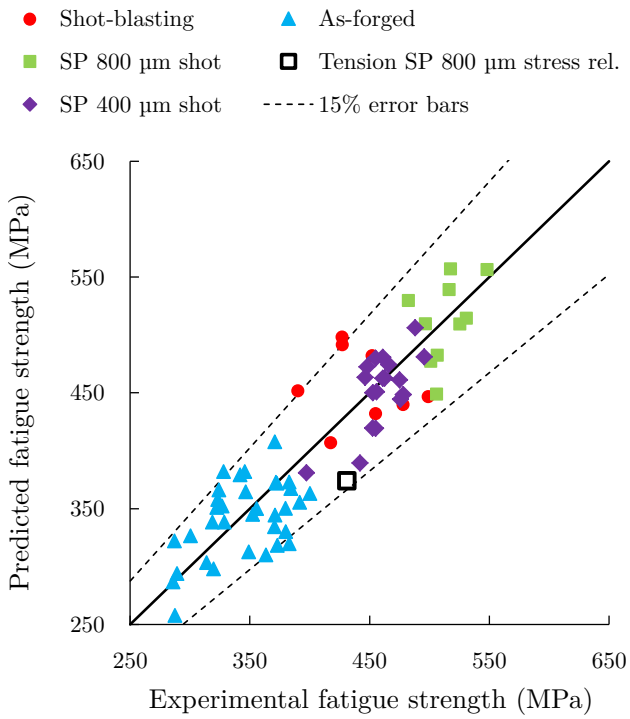

Fig. 15: Simulated fatigue strength versus experimental fatigue strength, for all critical defects.

having an error greater than 15%. This means that taking into account only the defect geometry and the residual stresses is enough to accurately predict the fatigue behaviour of a hot-forged and shot-blasted (or shot-peened) surface. It is important to note that the point for each batch are centred around the 1:1 line. This indicates that their dispersion is not due to the choice of parameters used for the simulations. Changing the (α, β) parameters to other values would not have improved the dispersion, as the parameters affect all points similarly. This is also true for the critical distance (figure 14): selecting a slightly different value would not have improved the dispersion and only changed the average error.

The model used here ignores the hardening introduced by shot-blasting and shot-peening. Taking this effect into account is possible and would mean changing the β value for each batch, leading to new α values. However, as stated previously, these new values would not improve the results, as the dispersion is due to the specimens themselves (defect geometry, surface integrity, etc.).

The simulations correctly reproduce the roughly 150 MPa difference in fatigue strength between the as-forged specimens and the shot-blasted (or shot-peened) specimens. This difference is due

to the effect of the residual stresses, their effective contribution to the Dang Van stress value is:

$$\Delta\sigma_{\text{eff}}^{\text{RS}} = \frac{\frac{\alpha}{3}\left(\sigma_{11}^{\text{RS}} + \sigma_{22}^{\text{RS}}\right)}{1/2 + \alpha/3} \tag{13}$$

The values for the effective contribution of the residual stresses for each batch are given in table table 2. Despite the different residual stress profiles, the residual stresses have similar

Stress in MPa	Shot-blasting	SP ∅800 µm shot	SP ∅400 µm shot
σ^{RS} at 40 µm depth	500	525	455
$\Delta\sigma_{\text{eff}}^{\text{RS}}$	152.5	160.2	135.8

Table 2: Effective contribution of the residual stresses to the fatigue strength, for each batch.

contributions for all batches. However, the 50 MPa difference between the two shot-peened batches seen in the experimental results (figure 3) is also present in the simulation results (figure 15), but is not matched by the difference in the contribution of the residual stresses. This means that the defect geometry is also contributing to the difference between the two batches. This is confirmed by calculating the K_f values of the defect geometry *without the residual stresses*: all batches have an average defect K_f value between 1.22 and 1.25, except for the shot-peened ∅800 µm shot which has an average defect K_f of 1.12. This difference is not due to defect size, as all batches have defects of similar sizes (figure 3). Furthermore, all shot-peened specimens were originally from the as-forged batch, and no particular selection was made when choosing which specimens were to be shot-peened. All batches should then have similar defects distributions, which means that the difference comes from the shot-peening itself. The large shot diameter could have a smoothing effect on defect geometry. This is not the case for the shot-peening with ∅400 µm shot, the shot diameter being twice as small means that a much smaller surface area is affected by each impact. The effect is also not observed for the shot-blasting despite using ∅1 mm shot. This is because the shots are not often changed and break or wear down to much smaller effective diameters. Furthermore, the critical defects of the shot-blasted specimens are extremely large, and the smoothing effect might not be as pronounced for defects of such size.

To illustrate this difference, simulations were performed with defects scanned before and after shot-peening. This analysis was not performed for shot-blasting as is was not possible to scan connecting rods before shot-blasting. Two defects of similar size and orientation were specifically chosen amongst the scanned surfaces. These are not critical defects, as the critical defects of these specimens were not similar enough for accurate comparison. The surface scans (before and after shot-peening) and the corresponding simulations are given in figure 16. Comparing the

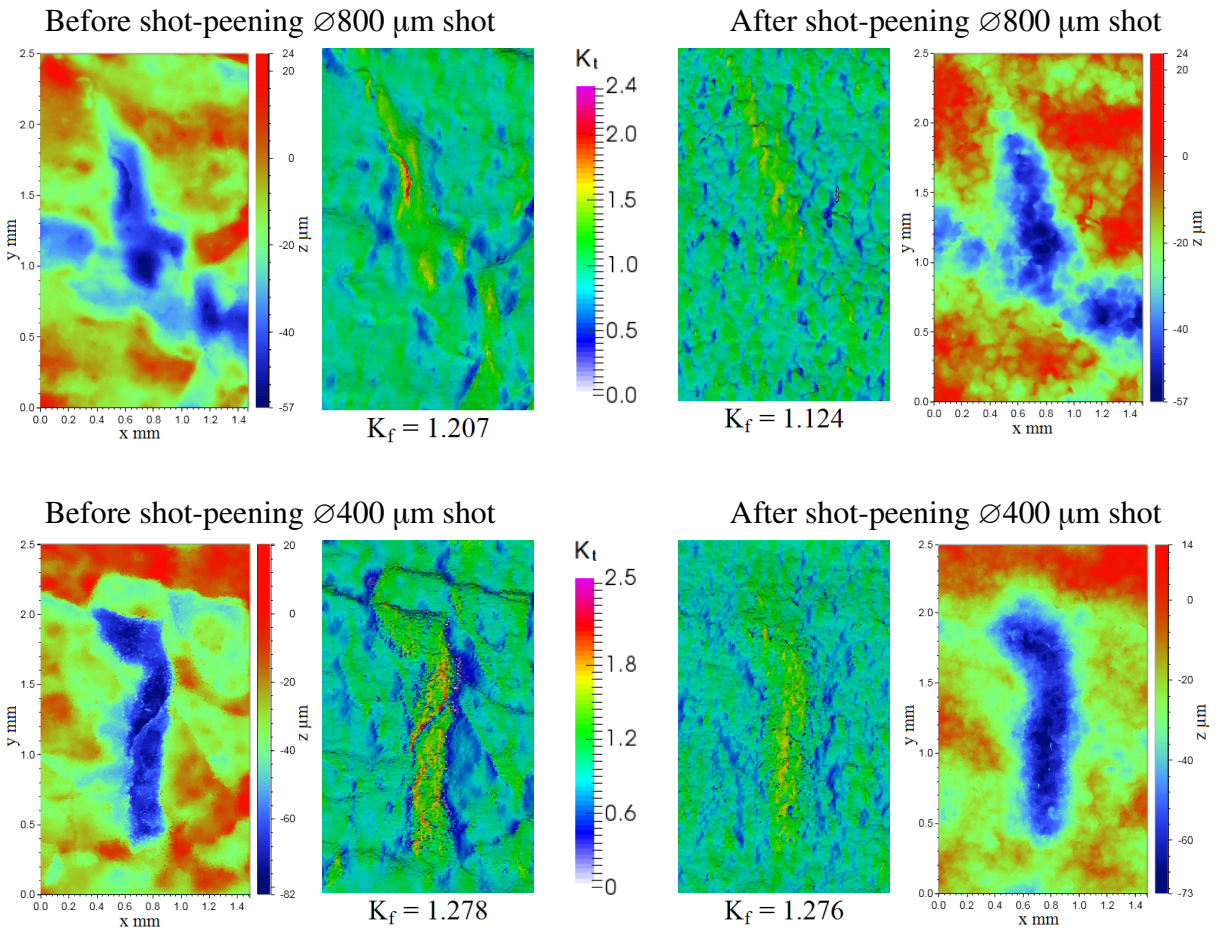

Fig. 16: Comparison of two defects, before and after shot-peening, for both shot-peened batches. The scanned surface and the corresponding surface K_t (FE simulation) are shown.

surface scans shows how the shot impacts have affected the defects: the general shape and the depth are unchanged but the edges are less clearly defined. The shot impacts also smooth out the local geometry: the maximum surface K_t is lower after shot-peening, for both batches. Figure 16

give the K_f values *without residual stresses* of the defects, before and after shot-peening. Before shot-peening, both defects have similar K_f values. However, after shot-peening, the K_f value is noticeably lower for the ∅800 µm shot while it remains unchanged for the ∅400 µm shot. This shows how the ∅800 µm shot seems to increase fatigue strength by reducing the impact of defect geometry.

Figure 17 plots the experimental fatigue limit versus the K_f value obtained with the FE simulation, taking into account both the defect geometry and the residual stresses. The data

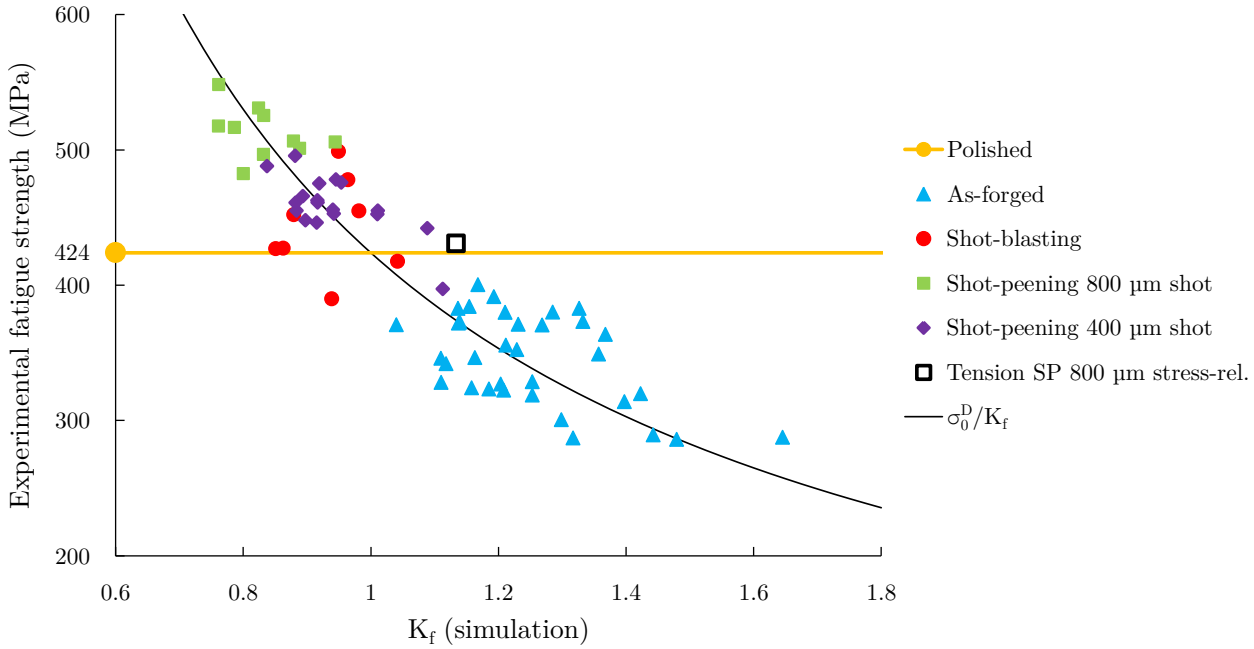

Fig. 17: Simulated fatigue strength versus experimental fatigue strength, for all critical defects.

points follow the curve $\sigma^D = \sigma_0^D / K_f$, which validates the simulations' K_f values.

5. Conclusion

The goal of this paper is to develop a fatigue approach which can take into account the combined effects of surface defects and shot-peening on fatigue behaviour. The components chosen for this study, hot-forged connecting rods, exhibit surface defects after forging and are subsequently shot-blasted. This study was performed on fatigue specimens machined out of hot-forged connecting rods. The specimens were thoroughly characterized and fatigue tests were then

performed to quantify the effect of the surface integrity on fatigue behaviour. The fatigue results show that the surface integrity has a major impact on fatigue behaviour: large forging defects and shot-blasting both affect fatigue strength. The two major aspects of the surface integrity are the forging defects and the residual stresses. The specimens were scanned before fatigue testing, so that the critical defects could be identified.

The fatigue results were analysed in order to develop a fatigue model, taking into account the surface integrity. Two approaches were used. The first is based on the fitting of the surface defects with an ellipsoid. This gives access to the defects' size and shape, allowing to quickly analyse a large number of defects. Combined with Peterson's K_t model, this method was able to detect the critical defect for roughly a third of all specimens.

The second model used FE simulations of the defects, in order to more accurately analyse the effect of their geometry. The theory of critical distance is used to quantify the influence of the defects and the residual stresses are taken into account with Dang Van's model. The simulations correctly predict the fatigue strength with at most 15% error. These results show that it is possible to accurately model the effect of the surface integrity using the following parameters:

- The material's reference fatigue strength
- The critical distance of the material
- The surface topography of the defects
- The residual stress profile

Despite the different profiles, the contribution of the residual stresses is almost the same for the shot-blasted and shot-peened batches. Additionally, the FE simulation approach showed that shot-peening with a large diameter shot can reduce the impact on fatigue of the forging defects.

Acknowledgements

This work has been performed within the ANR (National Research Agency) DEFISURF project, in a partnership including several industrial partners (Ascometal, CETIM, Renault, Transvalor, Atelier des Janves, Gévelot Extrusion) and academic institutions (INSA Lyon MATEIS, ENSMP-CEMEF, Arts et Métiers ParisTech LAMPA).

References

[1] Shahzad M., Chaussumier M., Chieragatti R., Mabru C., Rezai Aria F. (2010). Influence of anodizing process on fatigue life of machined aluminium alloy, Procedia Engineering, 2: 1015–1024.

[2] Chomienne V. (2014). Étude de l'influence de l'intégrité de surface en tournage de l'acier 15-5PH sur la tenue en fatigue en flexion rotative. PhD thesis, INSA, Lyon, France.

[3] Souto-Lebel A., Guillemot N., Lartigue C., Billardon R. (2011). Characterization and influence of defect size distribution induced by ball-end finishing milling on fatigue life, Procedia Engineering, V19.

[4] Shang D., Liu X., Shan Y., Jiang E. (2016). Research on the stamping residual stress of steel wheel disc and its effect on the fatigue life of wheel, International Journal of Fatigue, 93, 173–183.

[5] Dehmani H., Brugger C., Palin-Luc T., Mareau, C., Koechlin S. (2016). Experimental study of the impact of punching operations on the high cycle fatigue strength of Fe-Si thin sheets, International Journal of Fatigue, 82, 721-729.

[6] Murakami Y., Endo M. (1986). Effects of hardness and crack geometries on ΔK_{th} of small cracks emanating from small defects. In K. Miller & E. De Los Rios (Eds.), The Behaviour of Short Fatigue Cracks, 275–293. London: MEP Publications.

[7] Murakami Y. (2002). Metal fatigue: effects of small defects and non-metallics inclusion. London: Elsevier

[8] Billaudeau T., Nadot Y., Bezine G. (2004). Multiaxial fatigue limit for defective materials: mechanisms and experiments. Acta Mater, 52, 3911–20.

[9] Pessard E., Abrivard B., Morel F., Abroug F., Delhaye P. (2014). The effect of quenching and defects size on the hcf behaviour of boron steel. International Journal of Fatigue, 68(0), 80–89.

[10] Guerchais R., Saintier N., Morel F., Robert C. (2014). Micromechanical investigation of the influence of defects in high cycle fatigue, International Journal of Fatigue, 30, 2119-2126.

[11] Chantier I., Bobet V., Billardon R., Hild F. (2000). Probabilistic approach to predict the very high-cycle fatigue behaviour of spheroidal graphite cast iron structures Fatigue and Fracture of Engineering Materials and Structures 23 (2), pp. 173-180

[12] Nadot Y., Mendez J., Ranganathan N. (2004). Influence of casting defects on the fatigue limit of nodular cast iron, International Journal of Fatigue 26(3), 311-319

[13] Morel F., Morel A., Nadot Y. (2009). Comparison between defects and micro-notches in multiaxial fatigue - The size effect and the gradient effect, International Journal of Fatigue, 31(2), 263–275

[14] Koutiri I., Bellett D., Morel F., Augustins L., Adrien J. (2013). High cycle fatigue damage mechanisms in cast aluminium subject to complex loads. International Journal of Fatigue, 47, 44-57

[15] Le V.-D., Morel F., Bellett D., Saintier N., Osmond P. (2016). Simulation of the Kitagawa-Takahashi diagram using a probabilistic approach for cast Al-Si alloys under different multiaxial loads International Journal of Fatigue, 93, 109 – 121

[16] Serrano-Munoz I., Buffiere J.-Y., Verdu C., Gaillard Y.,, Mu P., Nadot Y. (2016]. Influence of surface and internal casting defects on the fatigue behaviour of A357-T6 cast aluminium alloy International Journal of Fatigue, 82, 361-370

[17] Léopold G., Nadot Y., Billaudeau T., Mendez J. (2015) Influence of artificial and casting defects on fatigue strength of moulded components in Ti-6Al-4V alloy, Fatigue and Fracture of Engineering Materials and Structures

[18] Gariépy A., Bridier F., Hoseini M., Bocher P., Perron C., Lévesque M. (2013). Experimental and numerical investigation of material heterogeneity in shot peened aluminium alloy AA2024-T351. Surface and Coatings Technology, 219(0), 15–30.

[19] Bhuiyan M. S., Mutoh Y., McEvily A. J. (2012). The influence of mechanical surface treatments on fatigue behavior of extruded az61 magnesium alloy. Materials Science and Engineering : A, 549(0), 69–75.

[20] McKelvey S. A., Fatemi A. (2012). Surface finish effect on fatigue behavior of forged steel. International Journal of Fatigue, 36(1), 130–145.

[21] Sakamoto J., Lee Y.-S., Cheong S.-K. (2014). Effect of fibprocessed sharp flaw on fatigue limit of shot peened medium carbon steel. In L. Wagner (Ed.), Proceedings of the 12th International Conference on Shot Peening , 86–89. Institute of Materials Science and Engineering.

[22] Sakamoto J., Lee Y.-S., Cheong S.-K. (2015). Effect of surface flaw on fatigue strength of shot-peened medium-carbon steel. Engineering Fracture Mechanics, 133, 99–111.

[23] Kim J. C., Cheong S. K., Noguchi H. (2013). Residual stress relaxation and low- and high-cycle fatigue behavior of shot-peened medium-carbon steel. International Journal of Fatigue, 114–122.

[24] Arola D., Ramulu M. (1999). An examination of the effects from surface texture on the strength of fiber reinforced plastics. Journal of Composite Materials, 33(2), 102–123.

[25] Peterson R. E. (1974). Stress Concentration Factors. New York: John Wiley and Sons.

[26] Suraratchai M., Limido J., Mabru C., & Chieragatti, R. (2008). Modelling the influence of machined surface roughness on the fatigue life of aluminium alloy. International Journal of Fatigue, 30(12), 2119–2126.

[27] Le Pécheur A., Curtit F., Clavela M., Stephan J.M., Reya C., Bompard Ph. (2012). Polycrystal modelling of fatigue: Pre-hardening and surface roughness effects on damage initiation for 304L stainless steel, International Journal of Fatigue, 45, 48–60

[28] Guilhem Y., Basseville S., Proudhon H., Cailletaud G. (2014). Effects of surface roughness on plastic strain localization in polycrystalline aggregates. 2nd International Symposium on Fatigue Design & Material Defects - FDMD II

[29] Kitagawa H., Takahashi S. (1976). Applicability of fracture mechanics to very small cracks or cracks in the early stage. In Proceedings of the second international conference on the mechanical behaviour of materials, 627–631. ASM.

[30] Fathallah, R., Laamouri, A., Sidhom, H., & Braham, C. (2004). High cycle fatigue behavior prediction of shot-peened parts. International Journal of Fatigue, 26(10), 1053–1067.

[31] Taylor D. (1999). Geometrical effects in fatigue : a unifying theoretical model. International Journal of Fatigue, 21(5), 413–420.

[32] Taylor D. (2007). The theory of critical distances: a new perspective in fracture mechanics. Amsterdam: Elsevier.

[33] Susmel L. (2008). The theory of critical distances: a review of its applications in fatigue. Engineering Fracture Mechanics, 75, 1706–1724.

[34] Taylor D. (2011). Applications of the theory of critical distances in failure analysis. Engineering Failure Analysis, 18, 543–549.

[35] Taylor D., Barrett N., Lucano G. (2002). Some new methods for predicting fatigue in welded joints. International Journal of Fatigue, 24, 509–18.

[36] Crupi G., Crupi V., Guglielmino E., Taylor D. (2005). Fatigue assessment of welded joints using critical distance and other methods. Engineering Failure Analysis, 12, 129–42.

[37] Araújo J.A., Susmelb L., Piresa M.S.T., Castro F.C. (2017). A multiaxial stress-based critical distance methodology to estimate fretting fatigue life. Tribology International, 108, 2–6.

[38] Zheng X., Cui H., Sub X., Engler-Pinto Jr. C.C., Wen W. (2013). Numerical modeling of fatigue crack propagation based on the theory of critical distances. Engineering Fracture Mechanics, 114, 151–165.

[39] El May M., Saintier N., Palin-Luc T., Devos O. (2015). Non-local high cycle fatigue strength criterion for metallic materials with corrosion defects. Fatigue Fract Engng Mater Struct, 38, 1017–1025

[40] Herasymchuk O.M., Kononuchenko O.V., Bondarchuk V.I. (2015). Fatigue life calculation for titanium alloys considering the influence of microstructure and manufacturing defects. International Journal of Fatigue, 81, 257–264.

[41] Benedetti M., Fontanari V., Allahkarami M., Hanan J.C., Bandini M. (2016). On the combination of the critical distance theory with a multiaxial fatigue criterion for predicting the fatigue strength of notched and plain shot-peened parts. International Journal of Fatigue, 93, 133–147.

[42] Morançais A. (2016). Effet du grenaillage sur la durée de vie des aubes monocristallines de turbine. PhD thesis, ONERA, Châtillon, France.

[43] Gerin B., Pessard E., Morel F., Verdu C. (2017). Influence of surface integrity on the fatigue behaviour of a hot-forged and shot-peened C70 steel component, Materials Science & Engineering A, 686, 121–133.

[44] Gumbel E. J. (1958). Statistics of Extremes. New York : Columbia University Press.

[45] Murakami Y., Usuki H. (1989). Quantitative evaluation of effects of non-metallic inclusions on fatigue strength of high strength steels. ii : Fatigue limit evaluation based on statistics for extreme values of inclusion size. International Journal of Fatigue, 11(5), 299–307.

[46] Geuzaine C., Remacle J.-F. (2009). Gmsh : a threedimensional finite element mesh generator with built-in pre- and post-processing facilities. International Journal for Numerical Methods in Engineering, 79(11), 1309–1331.

[47] Robert C., Mareau C. (2015). A comparison between different numerical methods for the modeling of polycrystalline materials with an elastic–viscoplastic behavior. Computational Materials Science, 103, 134–144.

[48] Dang Van K. (1993). Macro-micro approach in high-cycle multiaxial fatigue. In D. McDowell & J. Ellis (Eds.), Advances in Multiaxial Fatigue, 120–130. American Society for Testing and Materials. ASTM STP1191.

List of figure captions

Fig. 1: a) Connecting rod with spark-machined specimen. b) Example of a critical defect on an as-forged specimen. [43]

Fig. 2: Residual stress profiles for the various batches, in the direction of the specimen axis (long.), and the transverse direction (tvs.). [43]

Fig. 3: Kitagawa diagram of the fatigue tests, with fatigue strength and critical defect size of each valid specimen. [43]

Fig. 4: Diagram of a surface with a defect (green) and the corresponding ellipsoid (blue). The grid is the reference plane.

Fig. 5: Example of a surface defect (green) with the fitted ellipsoids (blue and red). The values for the semi-axes a and b are given in pixels (1 pixel = 3.5 µm) and the values for c are in µm.

Fig. 6: $\sqrt{area}$ of the defects from the as-forged specimens. For each specimen, the blue point are the defects and the critical defect is marked in red.

Fig. 7: Peterson's K_t of each defect for all specimens. For each specimen, the blue point are the defects and the critical defect is marked in red.

Fig. 8: Plots versus the standardised variable of the critical defects' K_t and depth values. The K_t values follow a Gumbel distribution (straight line), but the depth does not.

Fig. 9: Close-up of the mesh showing the element size gradient. a) Mesh gradient along the entire thickness. b) Mesh gradient in the first 100 µm, surface is marked in orange.

Fig. 10: Loading conditions of the FE simulations.

Fig. 11: Process for performing the FE simulations of the critical defects.

Fig. 12: FE simulation of a critical defect compared to its surface scan. Indicated on the scan are the defects' K_t value, calculated using the geometrical analysis.
Fig. 13: Cross-section of the FE simulation of the critical defect in figure 12. Stress values are in MPa, the white dot locates the maximum stress. The point method (red dot) and volume method (sphere centred on the white dot) are indicated.
Fig. 14: Stress gradients below the maximum stress for all critical defects of the as-forged specimens. Depth is relative: for each gradient, 0 depth is the tip of the defect.
Fig. 15: Simulated fatigue strength versus experimental fatigue strength, for all critical defects.
Fig. 16: Comparison of two defects, before and after shot-peening, for both shot-peened batches. The scanned surface and the corresponding surface K_t (FE simulation) are shown.
Fig. 17: Simulated fatigue strength versus experimental fatigue strength, for all critical defects.

List of table captions

Table. 1: Overview of the number of valid tests and fatigue strength range for each batch. [43]
Table. 2: Effective contribution of the residual stresses to the fatigue strength, for each batch.